Low-rate firing limit for neurons with axon, soma and dendrites driven by spatially distributed stochastic synapses

Robert P. Gowers[1], Yulia Timofeeva[2,4], Magnus J. E. Richardson[3],

1 Mathematics for Real-World Systems Centre for Doctoral Training, University of Warwick, Coventry, CV4 7AL, United Kingdom
2 Department of Computer Science, University of Warwick, Coventry, CV4 7AL, United Kingdom
3 Warwick Mathematics Institute, University of Warwick, Coventry, CV4 7AL, United Kingdom
4 Department of Clinical and Experimental Epilepsy, UCL Queen Square Institute of Neurology, University College London, London, WC1N 3BG, United Kingdom

* r.gowers@warwick.ac.uk

Abstract

Analytical forms for neuronal firing rates are important theoretical tools for the analysis of network states. Since the 1960s, the majority of approaches have treated neurons as being electrically compact and therefore isopotential. These approaches have yielded considerable insight into how single-cell properties affect network activity; however, many neuronal classes, such as cortical pyramidal cells, are electrically extended objects. Calculation of the complex flow of electrical activity driven by stochastic spatio-temporal synaptic input streams in these structures has presented a significant analytical challenge. Here we demonstrate that an extension of the level-crossing method of Rice, previously used for compact cells, provides a general framework for approximating the firing rate of neurons with spatial structure. Even for simple models, the analytical approximations derived demonstrate a surprising richness including: independence of the firing rate to the electrotonic length for certain models, but with a form distinct to the point-like leaky integrate-and-fire model; a non-monotonic dependence of the firing rate on the number of dendrites receiving synaptic drive; a significant effect of the axonal and somatic load on the firing rate; and the role that the trigger position on the axon for spike initiation has on firing properties. The approach necessitates only calculating first and second moments of the non-thresholded voltage and its rate of change in neuronal structures subject to spatio-temporal synaptic fluctuations. The combination of simplicity and generality promises a framework that can be built upon to incorporate increasing levels of biophysical detail and extend beyond the low-rate firing limit treated in this paper.

Author summary

Neurons are extended cells with multiple branching dendrites, a cell body and an axon. In an active neuronal network, neurons receive vast numbers of incoming synaptic pulses throughout their dendrites and cell body that each exhibit significant variability in amplitude and arrival time. The resulting synaptic input causes voltage fluctuations

throughout their structure that evolve in space and time. The dynamics of how these signals are integrated and how they ultimately trigger outgoing spikes have been modelled extensively since the late 1960s. However, until relatively recently the majority of the mathematical formulae describing how fluctuating synaptic drive triggers action potentials have been applicable only for small neurons with the dendritic and axonal structure ignored. This has been largely due to the mathematical complexity of including the effects of spatially distributed synaptic input. Here we show that in a physiologically relevant, low-firing-rate regime, an approximate, level-crossing approach can be used to provide an estimate for the neuronal firing rate even when the dendrites and axons are included. We illustrate this approach using basic neuronal morphologies that capture the fundamentals of neuronal structure. Though the models are simple, these preliminary results show that it is possible to obtain useful formulae that capture the effects of spatially distributed synaptic drive. The generality of these results suggests they will provide a mathematical framework for future studies that might require the structure of neurons to be taken into account, such as the effect of electrical fields or multiple synaptic input streams that target distinct spatial domains of cortical pyramidal cells.

Introduction

Due to their extended branching in both dendritic and axonal fields many classes of neurons are not electrically compact objects, in that the membrane voltage varies significantly throughout their spatial structure. A case in point are the principal, pyramidal cells of the cortex that feature a long apical dendritic trunk, oblique dendrites, apical tuft dendrites and a multitude of basal dendrites. Excitatory synapses are typically located throughout the dendritic arbour [1], while inhibitory synapses are clustered at specific regions depending on the presynaptic cell type [2]. These cells also differ morphologically not only between different layers, but also between cells in the same layer and class [3, 4]. Most cortical pyramidal cells *in vivo* fire rarely and irregularly due to the stochastic and balanced nature of the synaptic drive [5, 6]. Despite the apparent irregular firing of single neurons, computational processes are understood to be distributed across the population [7, 8] with the advantage that encoding information at a low firing rate can be energy efficient [9].

The arrival of excitatory and inhibitory synaptic pulses increases or decreases the postsynaptic voltage as well as increasing the conductance locally for a short time. Together with the spatio-temporal voltage fluctuations caused by the distributed synaptic bombardment typical of *in vivo* conditions, the increase in membrane conductance affects the integrative properties of the neuron, with reductions of the effective membrane time constant, electrotonic length constant and overall input resistance of neuronal substructures [10–12].

How different classes of neurons integrate stochastic synaptic input has been a subject of intense experimental [7, 13, 14] and theoretical [15–19] focus over the last 50 years. The majority of analytical approaches have approximated the cell as electrotonically compact and focussed on the combined effects of stochastic synaptic drive and intrinsic ion currents on the patterning of the outgoing spike train. Such models usually utilise an integrate-and-fire (IF) mechanism with some variations, and have been analysed using a Fokker-Planck approach [20–23] in the limit of fast synapses. However, this approach becomes unwieldy when synaptic filtering is included (though see [24–26]). One approximate analytical methodology, applicable to the low-firing-rate limit driven by filtered synapses is the level-crossing method of Rice [27]. In this approach, which has already been applied to compact neurons [28, 29], a system without post-spike reset is considered with the rate that the threshold is crossed from below

treated as a proxy for the firing rate; the upcrossing rate and firing rate for a system with reset will be similar when the rate is low.

Due partly to the sparsity of the experimental data required for model constraint, but also because of the mathematical complexity involved, few analytical results regarding stochastic synaptic integration are available for neurons with dendritic structure, excepting the work of Tuckwell [30–32]. Nevertheless there is increasing interest in the integrative and firing response of spatial neuron models [33, 34], for neurons subject to and generating electric fields [35–37] or the effect of axonal load and position of the action-potential initiation region [34, 38–42]. Advances in optogenetics and multiple, parallel intracellular recordings have made experimental measurement and stimulation of *in vivo*-like input at arbitrary dendritic locations feasible [43–45]. This potential for model constraint suggests it is timely for a concerted effort to extend the analytical framework developed for compact models driven by stochastic synapses to neurons with dendrites, soma and axon in which the voltage fluctuates in both space and time.

Here we detail an analytical framework for approximating the firing rate of neurons with a spatially extended structure in a physiologically relevant low-rate regime [46–48]. To illustrate the approach we applied it to simple but exemplary neuronal geometries with increasing structural features - multiple dendrites, soma and axon - and investigated how various morphological parameters including the electrotonic length, axonal radius, number of dendrites and soma size affect the firing properties.

Materials and Methods

Derivation of the stochastic cable equation

The cable equation for the voltage $V(x,t)$ in a dendrite of constant radius a and axial resistivity r_a with leak and synaptic currents has the form

$$c_{\mathrm{m}}\frac{\partial V}{\partial t} = g_L(E_L - V) + g_s(x,t)(E_s - V) + \frac{a}{2r_{\mathrm{a}}}\frac{\partial^2 V}{\partial x^2} \tag{1}$$

where c_{m}, g_L and g_s are the membrane capacitance, leak conductance and synaptic conductance per unit area respectively, while E_L and E_s are the equilibrium potentials for the leak and synaptic currents. The synaptic conductance over a small area of dendrite, $2\pi a\Delta_x$, at location x along the dendrite increases instantaneously by an amount γ_s for each incident synaptic input and then decays exponentially with time constant τ_s as the constituent channels close

$$2\pi a\Delta_x\tau_s\frac{\partial g_s}{\partial t} = -2\pi a\Delta_x g_s(x,t) + \gamma_s\tau_s\sum_{\{t_{sk}\}}\delta(t - t_{sk}). \tag{2}$$

Here $\{t_{sk}\}$ denotes the set of synaptic arrival times at location x. Each synaptic pulse is assumed to arrive independently, where the number that arrive in a time window Δ_t is Poisson distributed with a mean N_s given in terms of the dendritic section area, areal density of synapses ϱ_s, and mean synaptic arrival rate r_s

$$N_s = 2\pi a\Delta_x\varrho_s r_s\Delta_t. \tag{3}$$

Note that for a Poisson process the variance will also be N_s.

Gaussian approximation for the fluctuating conductance

For a high synaptic-arrival rate we can approximate the Poissonian impulse train by a Gaussian random number with mean N_s/Δ_t and standard deviation $\sqrt{N_s}/\Delta_t$ (this is an

extension to spatio-temporal noise of the approach taken in [20]). Dividing Eq (2) by the unit of membrane area and introducing ψ as a zero-mean, unit-variance Gaussian random number allows us to write

$$\tau_s \frac{\partial g_s}{\partial t} \approx -g_s + \tau_s \gamma_s r_s \varrho_s + \tau_s \gamma_s \sqrt{\frac{\varrho_s r_s}{2\pi a \Delta_x \Delta_t}} \psi, \tag{4}$$

where the right-hand side should be interpreted as having been discretized over time, with a time step Δ_t. We now define the space-time white-noise process $\xi(x,t) = \psi/\sqrt{\Delta_x \Delta_t}$ that has the properties

$$\langle \xi(x,t) \rangle = 0 \quad \text{and} \quad \langle \xi(x,t)\xi(x',t') \rangle = \delta(x-x')\delta(t-t') \tag{5}$$

and also note that in the steady state $\langle g_s \rangle = \tau_s \gamma_s r_s \varrho_s$. Returning to the cable equation, we split g_s and V into mean and fluctuating components with $g_s = \langle g_s \rangle + g_{sF}$ and $V = \langle V \rangle + v_F$, giving the equation for the mean components as

$$c_\mathrm{m} \frac{\partial \langle V \rangle}{\partial t} = g(E - \langle V \rangle) + \frac{a}{2r_\mathrm{a}} \frac{\partial^2 \langle V \rangle}{\partial x^2} \tag{6}$$

with $g = g_L + \langle g_s \rangle$ and $E = (g_L E_L + \langle g_s \rangle E_s)/g$. It is useful to introduce the time and space constants

$$\tau_v = \frac{c_\mathrm{m}}{g} \quad \text{and} \quad \lambda = \sqrt{\frac{a}{2g r_\mathrm{a}}}. \tag{7}$$

For the fluctuating component we assume that the product $g_{sF} v_F$ is small and obtain

$$c_\mathrm{m} \frac{\partial v_F}{\partial t} \approx -g v_F + g_{sF}(E_s - \langle V \rangle) + \frac{a}{2r_\mathrm{a}} \frac{\partial^2 v_F}{\partial x^2}. \tag{8}$$

Rescaling synaptic variables $s = g_{sF}(E_s - \langle V \rangle)$ and $\sigma_s = \frac{1}{2}\gamma_s (E_s - \langle V \rangle)\sqrt{\varrho_s r_s \tau_s/(2\pi a \lambda)}$ results in the following form for the synaptic equation

$$\tau_s \frac{\partial s}{\partial t} = -s + 2\sigma_s \sqrt{\lambda \tau_s}\, \xi(x,t). \tag{9}$$

The deterministic voltage $\langle V \rangle$ is generally spatially varying. However, if the synaptic equilibrium potential E_s is far from the effective resting voltage E and the fluctuating voltage remains close to E then it is reasonable to approximate the noise σ_s as being spatially uniform with $E_s - \langle V \rangle \approx E_s - E$. This is applicable for mostly excitatory synaptic drive where $E_s \sim 0$mV and $E \sim -60$mV. Letting $v = \langle V \rangle - E_L + v_F$, $\mu = E - E_L$, and substituting in τ_v and λ, we combine Eqs (6, 8) and (9) to obtain the stochastic cable equation used in the paper

$$\tau_v \frac{\partial v}{\partial t} = \mu - v + \lambda^2 \frac{\partial^2 v}{\partial x^2} + s. \tag{10}$$

Here μ and s comprise the constant and fluctuating inputs to the dendrite. These subthreshold dynamics are supplemented by the standard integrate-and-fire threshold-reset mechanism at a trigger position x_th; when the voltage at x_th exceeds a threshold v_th the voltage in the entire structure is reset to voltage v_re. Under *in vivo* conditions the action-potential will back-propagate throughout the neuron with complex spatio-temporal dynamics [49–51]; however, here we are considering the low-rate case in which these transient post-spike dynamics will have dissipated before the next action potential is triggered.

Boundary conditions

The morphologies explored in this paper are shown in Fig 1a and feature boundary conditions in which multiple dendrites and an axon meet at a soma. To account for these conditions we first define the axial current I_a in a cable, writing it in terms of the input conductance of an infinite cable $G_\lambda = 2\pi a\lambda g$,

$$I_a(x,t) = -\lambda G_\lambda \frac{\partial v}{\partial x}. \tag{11}$$

For a sealed end at $x = 0$, represented by a horizontal line in Fig 1a, no axial current flows out of the cable giving the boundary condition

$$\left.\frac{\partial v}{\partial x}\right|_{x=0} = 0. \tag{12}$$

When the cable is unbounded and semi-infinite in extent, as shown by two small parallel lines in Fig 1a, we apply the condition that the potential must be finite at all positions,

$$|v(x,t)| < \infty, \quad \text{for all } x,t. \tag{13}$$

For other cases, multiple (n) neurites join at a nominal soma $x=0$ which is treated as having zero conductance - these cases are shown by a small circle in Fig 1a. Under these conditions the voltage is continuous at the soma $v_1(0) = ... = v_n(0)$ and axial current is conserved

$$\sum_{k=1}^{n} \lambda_k G_{\lambda_k} \left.\frac{\partial v_k}{\partial x_k}\right|_{x_k=0} = 0, \tag{14}$$

where k identifies the kth of the n neurites and G_{λ_k} is its input conductance. Note that for each neurite the spatial variable x_k increases away from the point of contact $x_k = 0$. The addition of an axon changes this boundary condition by adding a cable of index α with length constant λ_α and conductance G_{λ_α}. Finally, when the soma at $x = 0$ is electrically significant (denoted by a large circle in Fig 1a), there is an additional leak and capacitive current at $x = 0$. This results in a current-conservation condition

$$\tau_0 \frac{dv_0}{dt} = -v_0 + \sum_{k=\alpha,1}^{n} \rho_k \lambda_k \left.\frac{\partial v_k}{\partial x_k}\right|_{x_k=0}, \tag{15}$$

where the subscript 0 denotes somatic quantities and the neurite dominance factor ρ_k, which is the conductance ratio between an electrotonic length of cable and the soma [52] is $\rho_k = G_{\lambda_k}/G_0$. As in the case for the nominal soma, the other condition is that the voltage is continuous.

Numerical simulation

The cable equations for each neurite with a threshold-reset mechanism were numerically simulated by implementing the Euler-Maruyama method by custom-written code in the Julia language [53]. We discretized space and time into steps Δ_x and Δ_t, with v and s measured at half-integer spatial steps and the derivative $\partial v/\partial x$ at integer spatial steps. Hence, denoting k as the spatial index and i as the temporal index such that $(x,t) = (k\Delta_x, i\Delta_t)$, $v((k+\frac{1}{2})\Delta_x, i\Delta_t) = v^i_{k+1/2}$ and $\partial v/\partial v(k\Delta_x, i\Delta_t) = \partial_x v^i_k$. The numerical

algorithm used to generate v and s was therefore as follows

$$\begin{aligned} v^{i+1}_{k+1/2} &= v^{i}_{k+1/2} + \frac{\Delta_t}{\tau_v}\left[\mu - v^{i}_{k+1/2} + \frac{\lambda^2}{\Delta_x}(\partial_x v^{i}_{k} - \partial_x v^{i}_{k+1}) + s^{i}_{k+1/2}\right], \\ \partial_x v^{i+1}_{k} &= \frac{v^{i+1}_{k+1/2} - v^{i+1}_{k-1/2}}{\Delta_x}, \\ s^{i+1}_{k+1/2} &= s^{i}_{k+1/2} + \frac{\Delta_t}{\tau_s}\left(-s^{i}_{k+1/2} + 2\sigma_s\sqrt{\frac{\lambda\tau_s}{\Delta_x\Delta_t}}\psi^{i}_{k}\right), \end{aligned} \tag{16}$$

where ψ denotes a zero-mean, unit-variance Gaussian random number. The code used to generate the figures is provided in the supplementary information [54]. When the approximation of an infinite or semi-infinite neurite was required, the length L was chosen to be sufficiently large such that boundary effects were negligible ($L = 1000\mu$m or greater). To ensure stability of the differential equation, for a spatial step of $\Delta_x = 20\mu$m, we used a time step of $\Delta_t = 0.02$ ms. We verified that this step size was sufficiently small in comparison to the values of λ used by running simulations at smaller Δ_x and checking for convergence.

Results

Before examining more complex spatial models with multiple dendrites, soma and axon, we first review the subthreshold properties of a single closed dendrite driven by fluctuating, filtered synaptic drive. We then illustrate how the upcrossing method can be applied to spatial models by interpreting the results for the closed dendrite as either a long dendrite with a nominal soma at one end or as two long dendrites meeting at a nominal soma. More complex neuronal geometries are then considered including those with multiple dendrites, axon and an electrically significant soma. The parameter ranges used are given in the Appendix in Table S1.

Subthreshold properties of a closed dendrite

The dendrites considered here are driven by distributed, filtered synaptic drive. For reasons of analytical transparency, excitatory and inhibitory fluctuations are lumped into a single drive term $s(x,t)$, though it is straightforward to generalise the synaptic fluctuations to two distinct processes. The fluctuating component of the synaptic drive obeys the following equation

$$\tau_s \frac{\partial s}{\partial t} = -s + 2\sigma_s\sqrt{\lambda\tau_s}\,\xi(x,t) \tag{17}$$

parametrized by a filter time constant τ_s, amplitude σ_s and driven by spatio-temporal Gaussian white noise $\xi(x,t)$ (see Materials and Methods for links to underlying presynaptic rates and density, as well as the autocovariance of $\xi(x,t)$). Note that the fluctuating component of the synaptic drive $s(x,t)$ is a temporally filtered but spatially white Gaussian process. The subthreshold voltage in the dendrite, driven by these synaptic fluctuations, will also be a fluctuating Gaussian process and obeys the following equation

$$\tau_v \frac{\partial v}{\partial t} = \mu - v + \lambda^2\frac{\partial^2 v}{\partial x^2} + s, \tag{18}$$

where the time constant τ_v and electrotonic length constant λ are reduced by the tonic conductance increase coming from the mean component of the synaptic drive (again, see

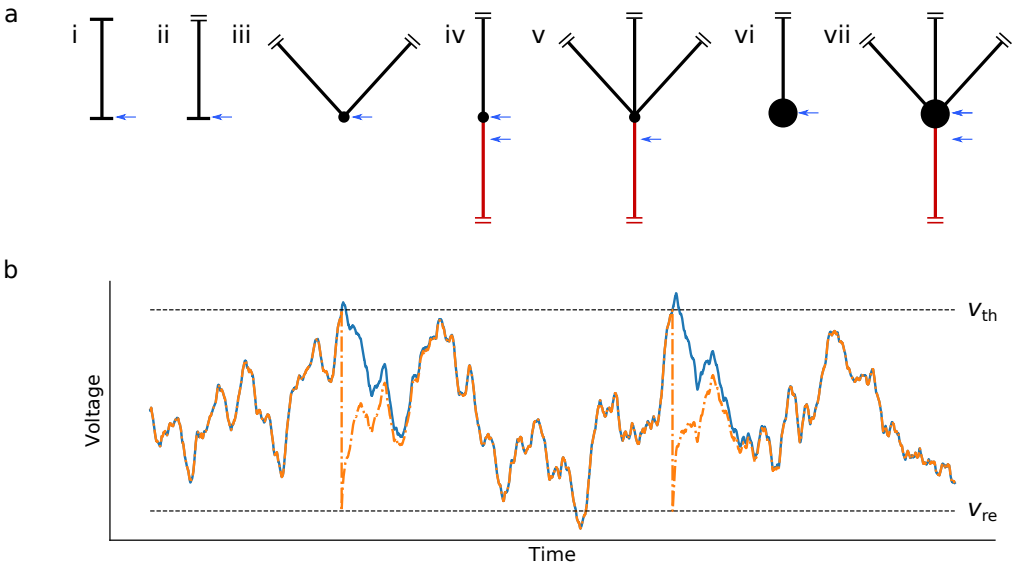

Fig 1. (a) The morphologies examined in this paper: (i) closed dendrite, (ii) semi-infinite one-dendrite model, (iii) two-dendrite model, (iv) dendrite and axon, (v) multiple dendrites and axon, (vi) dendrite and soma, (vii) multiple dendrites, soma and axon. Long black lines denote dendrites, red lines indicate the axon, while the blue arrows indicate the different spike trigger positions used. The symbols in the diagrams illustrate the following features: horizontal line - sealed end, two parallel lines - semi-infinite cable, small circle - nominal soma, and large circle - electrically significant soma. (b) Illustration of the upcrossing approximation. If the time between firing events is long compared to the relaxation time, the voltage without reset (solid blue line) will converge to the voltage of a threshold-reset process (orange dashed line) for the same realisation of stochastic drive. Under these conditions the upcrossing and firing-rates for the two processes are comparable.

Materials and Methods for derivation) and μ is the effective resting potential. For a closed dendrite of length L, shown in Fig 1a (i), there are two additional zero spatial-gradient conditions on $v(x,t)$ at $x=0,\ L$, Eq (12). With these definitions, it is straightforward to derive moments of the voltage using Green's functions Eq (S21) into Eq (S14). The resulting second moments can then be more succinctly written by defining the function

$$C(x,\eta) = \frac{\cosh((L-x)\sqrt{\eta}/\lambda)\cosh(x\sqrt{\eta}/\lambda)}{\sqrt{\alpha}\sinh(L\sqrt{\eta}/\lambda)}. \tag{19}$$

Hence in terms of this function $C(x,\eta)$, the variance is

$$\sigma_v^2(x) = \frac{2\sigma_s^2\tau_s}{\tau_v}\left\{C(x,1) - C(x,\kappa)\right\}, \tag{20}$$

where $\kappa = 1+\tau_v/\tau_s$. Similarly from Eq (S15), the variance of $\dot{v}$ is

$$\sigma_{\dot{v}}^2(x) = \frac{2\sigma_s^2}{\tau_v\tau_s}C(x,\kappa). \tag{21}$$

Note that the second term in the voltage-variance equation, Eq (20), and the variance of the voltage rate-of-change feature a second, shorter length constant $\lambda/\sqrt{\kappa}$ that is a function of the ratio of voltage to synaptic time constants. As expected, Fig 2a shows

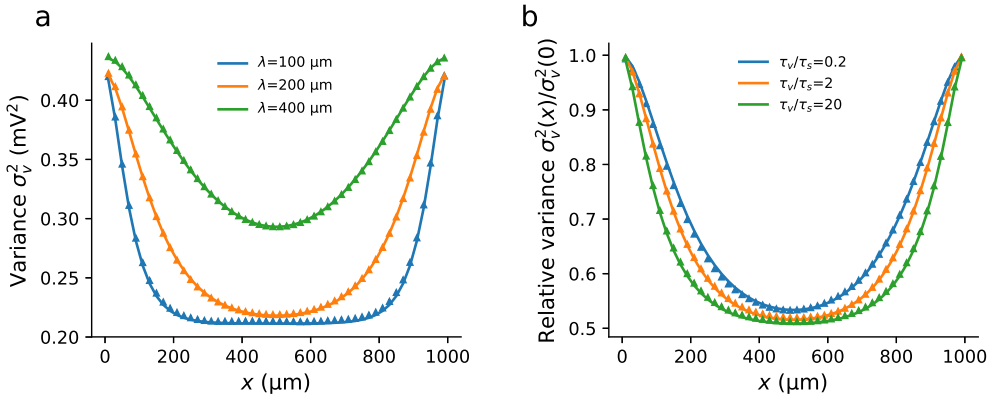

Fig 2. The variance profile in a sealed dendrite is a function of both the electrotonic length λ and ratio of synaptic to voltage time constants constant τ_s/τ_v. (a) The variance near the sealed end is higher than in the bulk with the extent of the boundary effect decreasing with λ. (b) Normalising the variance in the cable such that the variance at the ends is unity, it can be seen that increasing τ_v/τ_s decreases the effective length constant. For both plots the other parameters were $L = 1000\mu$m, $\tau_s = 5$ms, $\sigma_s = 1$mV. (a) $\tau_v = 10$ms, (b) $\lambda = 200\mu$m.

decreasing λ leading to a lower overall variance as well as a faster decay to the bulk properties from the boundaries. We also see from κ that the relative size of the time constants affects not just the magnitude of the variance but also its spatial profile. For higher τ_v/τ_s, σ_v^2 decreases at all positions and the profile decays faster to the bulk value as the second length constant decreases. By measuring $\sigma_v^2(x)$ relative to the variance at the ends Fig 2b shows the latter effect, though this reduction in the effective length constant by increasing τ_v/τ_s is not as significant as decreasing λ.

Note that for the cases where $\lambda/L \ll 1$, which is physiologically relevant for the high-conductance state, the influence of the boundary at L is negligible at $x = 0$ and at the midpoint there is little influence from either boundary. With this in mind, the morphologies treated in this paper comprise neurites that are treated as semi-infinite in length.

Firing rate approximated by the upcrossing rate

Full analytical solution of the partial differential Eqs (17, 18) when coupled to the integrate-and-fire mechanism does not appear trivial, even for the simple closed dendrite model. However, a level-crossing approach developed by Rice [27] and exploited in many other areas of physics and engineering, such as wireless communication channels [55], sea waves [56], superfluids [57] and grown-surface roughness [58] has previously been applied successfully to compact neuron models [28, 29] and can be extended to spatial models. The method provides an approximation for the mean first-passage time for any Gaussian process in which the mean $\langle v \rangle$, standard deviation σ_v, and rate-of-change standard deviation $\sigma_{\dot{v}}$ are calculable. The upcrossing rate is the frequency at which the trajectory of v without a threshold-reset mechanism crosses v_{th} from below (i.e. with $\dot{v} > 0$). Example voltage-time traces for the model with and without threshold are compared in Fig 1b. This approach provides a good approximation to the rate with reset when the firing events are rare and fluctuation driven, making it applicable to the physiological

low-rate firing regime. The upcrossing approximation to the firing rate is given by

$$r_{\rm uc} = \frac{1}{2\pi}\frac{\sigma_{\dot v}}{\sigma_v}\exp\left(-\frac{(v_{\rm th}-\langle v\rangle)^2}{2\sigma_v^2}\right) \tag{22}$$

where the statistical measures of the voltage are those at the trigger point $x_{\rm th}$. Note that because of the requirement that $\sigma_{\dot v}$ exists the upcrossing method cannot be applied to neurons driven by temporal white noise. However, it works well for coloured-noise drive, which is not directly tractable using standard Fokker-Planck approaches even for point-neuron models. The moments required for the upcrossing Eq (22) can be found using the Green's functions of the corresponding set of cable equations for a particular morphology and, since we only need the moments at $x_{\rm th}$, we only need the Green's function for the neurite that contains the trigger position (see Appendix for details). We now illustrate this using two interpretations of the closed dendrite model, the one-dendrite model which focuses on the behaviour at a sealed end - Fig 1a (ii) - and the two-dendrite model which focuses on the bulk - Fig 1a (iii).

One-dendrite and two-dendrite models

The method is first applied to a neuron with a single long dendrite and nominal soma (the trigger point $x=0=x_{\rm th}$) and axon, both of negligible conductance so that the end can be considered sealed. This corresponds to the $x<L/2$ half of the closed cable model considered above, in the limit that $L/\lambda\to\infty$. The second moments have already been calculated for the general case (Eqs 20, 21) so for $x_{\rm th}=0$ we have

$$\sigma_v^2 = \frac{2\sigma_s^2\tau_s}{\tau_v}\left(1-\frac{1}{\sqrt{\kappa}}\right) \quad\text{and}\quad \sigma_{\dot v}^2 = \frac{2\sigma_s^2}{\tau_s\tau_v}\left(\frac{1}{\sqrt{\kappa}}\right). \tag{23}$$

Substitution of these second moments into Eq (22) yields the upcrossing approximation to the firing rate for this geometry.

A second interpretation of the closed dendrite model is to place the trigger position in the middle $x_{\rm th}=L/2$ and then, in the limit $L/\lambda\to\infty$ consider the halves as two dendrites with statistically identical properties radiating from a nominal soma and axon, again both with negligible conductance. Taking these limits of the closed-dendrite Eqs (20, 21) for this case generates second moments that happen to be exactly half that of the one-dendrite case

$$\sigma_v^2 = \frac{\sigma_s^2\tau_s}{\tau_v}\left(1-\sqrt{\frac{\tau_s}{\tau_s+\tau_v}}\right) \quad\text{and}\quad \sigma_{\dot v}^2 = \frac{\sigma_s^2}{\tau_s\tau_v}\sqrt{\frac{\tau_s}{\tau_s+\tau_v}}, \tag{24}$$

where here we have written the functional dependence of κ on τ_v and τ_s explicitly. Given that the voltage at $x_{\rm th}$ is affected by activity occurring within distances a few λ down attached dendrites (see Fig 2) it might reasonably be expected that the statistical quantities and therefore the firing rate at $x_{\rm th}$ would be dependent on the electronic length quantity λ. However, for both the one and two-dendrite models considered above it is clear that there is no λ dependence for the second moments. Though this is unavoidable on dimensional grounds, because in either case no other quantities carry units of length once the limit $L/\lambda\to 0$ has been taken, the result is nevertheless a curious one.

The upcrossing and firing rates as a function of μ for the two models are compared in Fig 3, with the deterministic firing rate also shown (this is equivalent to the deterministic rate of the leaky integrate-and-fire model). Note that we keep τ_v and λ constant across the range of μ since these parameters would change little across the range of mean synaptic drive we investigate and it allows us to isolate the dependence of

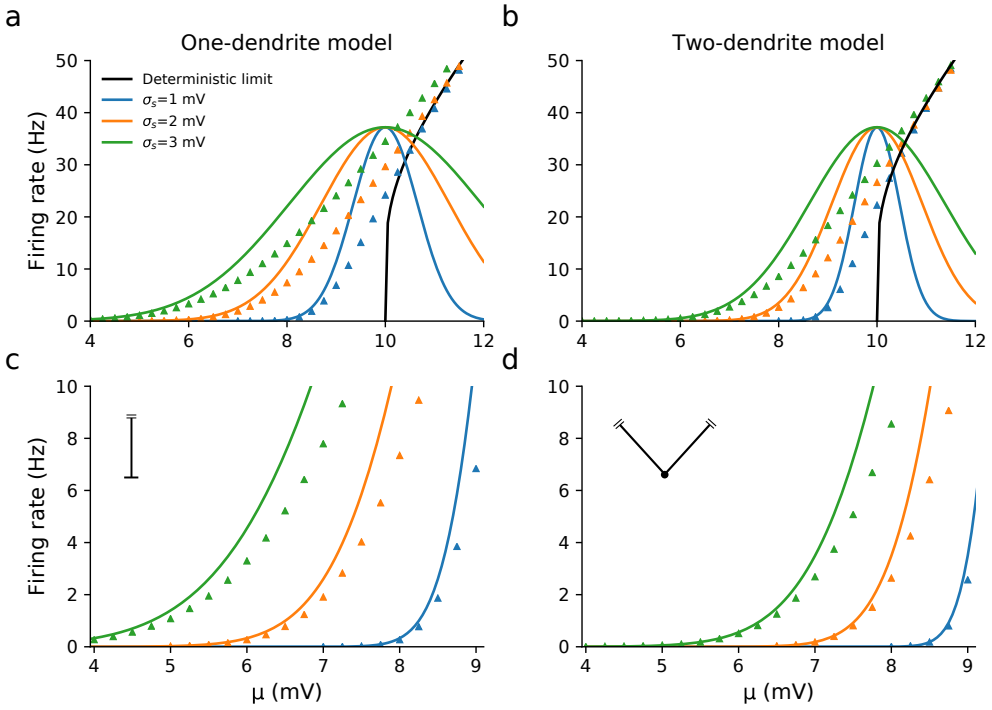

Fig 3. The firing rates of the one and two-dendrite models driven by spatially distributed, filtered stochastic synaptic drive for three fixed values of the fluctuation strength σ_s. While the firing rates of the one and two-dendrite models are similar in the suprathreshold regime (panels a and b, $\mu > 10$mV), the one-dendrite model has a higher firing rate in the subthreshold regime due to the variance being twice that of the two-dendrite model for the same value of σ_s. The upcrossing approximation is accurate when $(v_{\rm th} - \mu)/\sigma_v \gg 1$ (panels c and d). The other parameters used were $\lambda = 200\mu$m, $\tau_v = 10$ ms, $\tau_s = 5$ms, $v_{\rm th} = 10$mV, $v_{\rm re} = 0$mV.

the firing rate on just one parameter. The upcrossing rate provides a good approximation to the full firing rate at low rates in the < 5Hz range. In this way the upcrossing rate for spatio-temporal models provides a similar approximation to the firing rate as did the Arrhenius form derived by Brunel and Hakim [20] for the white-noise driven point-like leaky integrate-and-fire model.

Compared with the one-dendrite model, we see from Figs 3b and 3d that the firing rate for the two-dendrite model is significantly lower in the subthreshold regime but converges to the same value when μ goes above threshold. This illustrates that even simple differences in morphology affect stochastic and deterministic firing very differently. In addition Fig 4a shows that the firing rate is unaffected by the value of λ chosen, confirming by simulation the λ-independence of the firing rate. Furthermore when we choose the same value of σ_v for the one and two-dendrite models, then both the upcrossing rate and the simulated firing rates are the same, as seen in Fig 4b.

However, despite the independence of λ, the firing-rate profile for this toy model is distinct to that for the point-like leaky integrate-and-fire model, for which the second moments are $\sigma_v^2 \propto \tau_s/(\tau_s + \tau_v)$ and $\sigma_{\dot v}^2 \propto 1/[\tau_s(\tau_s + \tau_v)]$ [29]. This indicates that spatial structure by itself decreases the variance while increases derivative variance by a factor $\sqrt{1 + \tau_v/\tau_s} = \sqrt{\kappa}$. The moments also differ in their dependence on τ_v and τ_s from two-compartmental models [59].

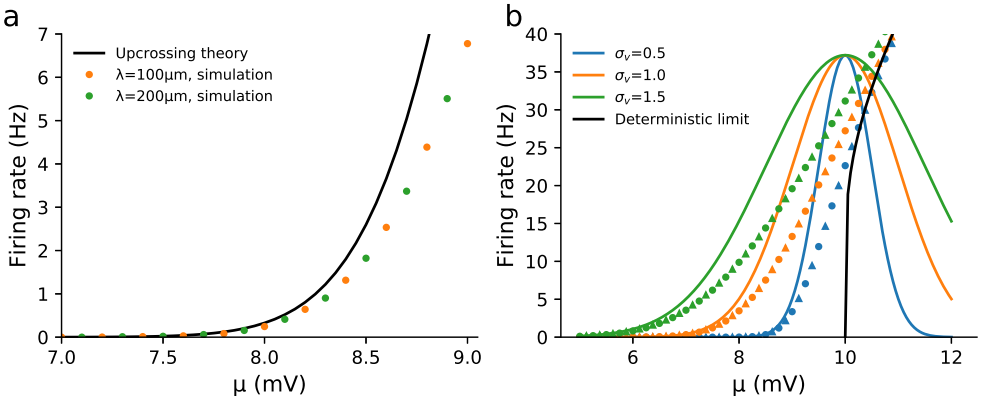

Fig 4. Independence of the firing rate on the electrotonic length λ for the one-dendrite model, and between the one and two-dendrite models for the same voltage variance. (a) The firing rate of the one-dendrite model with two different λ show it to be independent from λ, $\sigma_s = 1$mV. (b) If the synaptic fluctuation strength σ_s is adjusted such that the one and two-dendrite models have the same voltage variance σ_v^2 at the threshold position, then their upcrossing rates are identical. Simulations (circles and triangles for one and two-dendrite models respectively) suggest that the full firing rates are also independent of geometry in this case. The other parameters used were $\tau_v = 10$ms, $\tau_s = 5$ms, $v_{\rm th} = 10$mV and $v_{\rm re} = 0$mV.

Dendrite and axon

Next, we consider a dendrite connected to an axon at $x_1 = 0 = x_\alpha$, as shown in Fig 1a (iv), where dendritic and axonal quantities are denoted by subscripts 1 and α, respectively. This differs from the previous two-dendrite model as the axon receives no synaptic drive, so $\mu_\alpha = 0$ and $s_\alpha = 0$. Furthermore, intrinsic membrane properties of the axon (τ_α, λ_α) differ from the dendrite due to the smaller axonal radius and lack of synapse-induced increased membrane conductance [11,12]. Since $\mu_\alpha = 0$ we omit the subscript on the mean dendritic drive, $\mu_1 = \mu$. Taking the reasonable assumptions that the per area leakage capacitance and leak conductance are the same in the axon as the soma, we can calculate τ_α in terms of τ_1 given the mean level of synaptic drive (see Eqs (S39, S41)). Unlike the closed-dendrite models, the mean is no longer homogeneous in space due to the lack of synaptic drive in the axon. Defining $\tilde{f}_1(\omega)$ as the input admittance of the dendrite relative to the whole neuron,

$$\tilde{f}_1(\omega) = \frac{G_{\lambda_1}\gamma_1}{G_{\lambda_1}\gamma_1 + G_{\lambda_\alpha}\gamma_\alpha} = \frac{g_1^2\lambda_1^3\gamma_1}{g_1^2\lambda_1^3\gamma_1 + g_\alpha^2\lambda_\alpha^3\gamma_\alpha}, \tag{25}$$

where $\gamma_j = \sqrt{1 + i\omega\tau_j}$, we can show that the mean in the axon is given by (see Eq (S12))

$$\langle v(x_\alpha)\rangle = \tfrac{1}{2}\mu e^{-x_\alpha}\tilde{f}_1(0). \tag{26}$$

It is important to note that, unlike in the one and two-dendrite models, Eq (26) implies that it is now possible for the neuron to still be in the subthreshold firing regime when $\mu > v_{\rm th}$. In general, the second moments do not have a closed-form solution but can be expressed in terms of the angular frequency ω. It can be shown that the integrand for σ_v^2 and $\sigma_{\dot{v}}^2$ is proportional to $|\tilde{f}_1(\omega)|^2$, Eq (S38).

First we set the action-potential trigger position at $x_{\rm th} = 0$ and evaluated the effect of the axon by comparing the firing rate for the model with an axon, $r_{\rm axon}$, to the firing

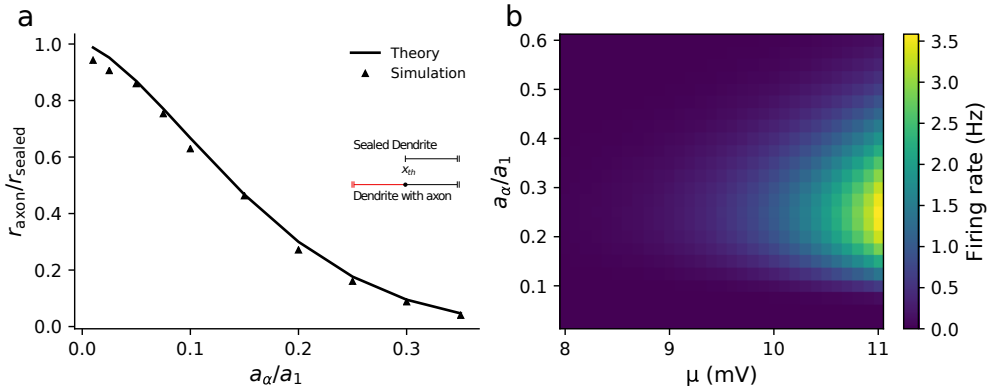

Fig 5. Addition of an axon significantly affects the firing rate even for small axonal conductance loads. (a) The axon increases the input conductance of the neuron, thereby lowering the firing rate for $x_{\rm th}=0$, $\mu=5$mV. (b) When $x_{\rm th}>0$ (here $x_{\rm th}=30\mu$m) the firing rate varies non-monotonically with the axonal radius and peaks at a physiologically reasonable value of the ratio of axon/dendrite radii for a range of synaptic parameters. The parameters used were $\lambda_1=200\mu$m, $\tau_s=5$ms, $\tau_1=10$ms, $\tau_\alpha=11.7$ms (calculated from Eq (S39)), $\sigma_s=3$mV, $v_{\rm th}=10$mV and $v_{\rm re}=0$mV.

rate of the one-dendrite model with a sealed end ($\partial v/\partial x=0$) at $x=0$, $r_{\rm sealed}$ (effectively an axon with zero conductance load). We also kept the noise strength σ_s rather than the voltage standard deviation σ_v fixed as we wished to see how the axon changes the variance of fluctuations at the trigger position. The relative firing rate was defined as $r_{\rm axon}/r_{\rm sealed}$. The ratio of the axonal to dendritic radius a_α/a_1 was varied and the relative firing rate calculated, with $a_\alpha/a_1=0$ being equivalent to no axon present. As illustrated in Fig 5a, the addition of a very low conductance or relatively thin axon significantly reduces the firing rate. This effect arises because the magnitude of $\tilde{f}_1(\omega)$ decreases at all frequencies for a larger radius ratio, which can be understood by recalling that $\lambda_j\propto\sqrt{a_j}$, Eq (7).

For cortical pyramidal cells, action potentials are typically triggered around $x_{\rm th}=30\mu$m down the axon in the axon initial segment [60–62]. It is straightforward to investigate the effect of moving the trigger position down the axon using the upcrossing approach. Interestingly, when $x_{\rm th}>0$, a non-monotonic relationship between the firing rate and radius ratio a_α/a_1 became apparent (see Fig 5b), with the peak ratio of ~ 0.25 being similar to that between the axonal initial segment and apical dendrite diameter in pyramidal cells [41, 63]. This is caused by a non-monotonic dependence of both $\langle v\rangle$ and σ_v^2 on a_α/a_1 for $x_{\rm th}>0$ with each peaking at intermediate values. Intuitively, this can be understood from the definition of λ_α, which increases as $\sqrt{a_\alpha}$. Thus the decay length of voltage fluctuations that enter the axon from the dendrite increases, increasing both $\langle v\rangle$ and σ_v^2 at $x_{\rm th}$. On the other hand, a larger λ_α increases the input conductance of the neuron, which, conversely, decreases $\langle v\rangle$ and σ_v^2. For smaller λ_α the decay length effect is more significant, whereas for larger λ_α the increase in input conductance plays a larger role.

Multiple dendrites and axon

We now consider a case with multiple dendrites and an axon radiating from a nominal soma (Fig 1a (v)). The dendrites are labelled $1, 2, ..., n$ with the axon labelled α as before. The dendrites have identical properties with independent and equally distributed synaptic drive. As in the previous case with the dendrite and axon, we kept

the synaptic strength σ_s fixed as we changed the number of dendrites. An immediate consequence of multiple dendrites is that, since $\mu > 0$ the mean voltage in the axon increases as more dendrites are added, with each contribution summing linearly,

$$\langle v_\alpha(x_\alpha)\rangle = \sum_{k=1}^{n} \langle v_{\alpha k}(x_\alpha)\rangle, \tag{27}$$

where $\langle v_{\alpha k}(x_\alpha)\rangle$ is the contribution to the axonal voltage mean from dendrite k. Introducing the relative input admittance of a single dendrite $\tilde{f}_n(\omega)$

$$\tilde{f}_n(\omega) = \frac{G_{\lambda_1}\gamma_1}{nG_{\lambda_1}\gamma_1 + G_{\lambda_\alpha}\gamma_\alpha} = \frac{g_1^2\lambda_1^3\gamma_1}{ng_1^2\lambda_1^3\gamma_1 + g_\alpha^2\lambda_\alpha^3\gamma_\alpha}, \tag{28}$$

it can be shown that when all dendrites have identical mean input drive μ, the mean in the axon is given by (see Eqs (S12, S23))

$$\langle v(x_\alpha)\rangle = \tfrac{1}{2}n\mu e^{-x_\alpha}\tilde{f}_n(0). \tag{29}$$

Thus we can see that as n increases the mean increases towards the constant value of $\frac{1}{2}\mu e^{-x_\alpha}$. However, this is not the case for the fluctuating component: despite more sources of fluctuating synaptic input both σ_v^2 and $\sigma_{\tilde{v}}^2$ in the axon decrease as $1/n$ for a large number of dendrites. We can see this by noting that for large n, $|\tilde{f}_n(\omega)|^2$ and hence the variance contribution from each dendrite scales as $1/n^2$. Therefore for n total dendrites, the total variance at x_{th} in the axon will scale as $1/n$ for large n. This reduction in axonal variance with additional dendrites is a generalisation of the reduction in variance we saw between the one and two-dendrite models earlier in Eqs (23, 24).

When it is the fluctuations that contribute significantly for firing (i.e. smaller μ or λ_α) then a reduction in variance from adding more dendrites will decrease the firing rate; however, when the mean is more significant (larger μ or λ_α) then the firing rate will increase as the number of dendrites increases. An example of the former case is shown in Fig 6a for $\lambda_\alpha = 100\mu$m, while an example of the latter is seen in Fig 6b for $\lambda_\alpha = 150\mu$m. The transition between these regimes can be seen in Fig 6c, which shows how the value of n that maximises the firing rate, $n_{\max}$, increases with μ and a_α/a_1. Physiologically, the reduction in variance is not simply the fact that adding dendrites increases cell size and thus input conductance, but that the relative conductance of each input dendrite to the total conductance decreases. Given that the total input conductance for n dendrites and an axon is

$$G_{\text{in}}(n) = n(2\pi a_1\lambda_1)g_1 + 2\pi a_\alpha\lambda_\alpha g_\alpha, \tag{30}$$

we can test this idea by scaling λ_1, a_1 with n (i.e. making the dendrites thinner) to keep the total input conductance the same as the single dendrite case, $G_{\text{in}}(n=1)$. This gives the simple relationship $\lambda_1(n) = \lambda_1(n=1)/n^{1/3}$, with which the segment factor is

$$\tilde{f}_n(\omega) = \frac{g_1^2\lambda_1^3(n=1)\gamma_1}{n(g_1^2\lambda_1^3(n=1)\gamma_1 + g_\alpha^2\lambda_\alpha^3\gamma_\alpha)}. \tag{31}$$

Since the integrands for the second moments are proportional to $|\tilde{f}_n(\omega)|^2$ (see Eq (S38)), this shows that second moments and hence the firing rate for fixed λ_α still decrease with n (see Fig 6d).

Dendrites, soma and axon

We now consider the case illustrated in Fig 1a (vii), where the electrical properties of the soma are non-negligible with its lumped capacitance and conductance providing an

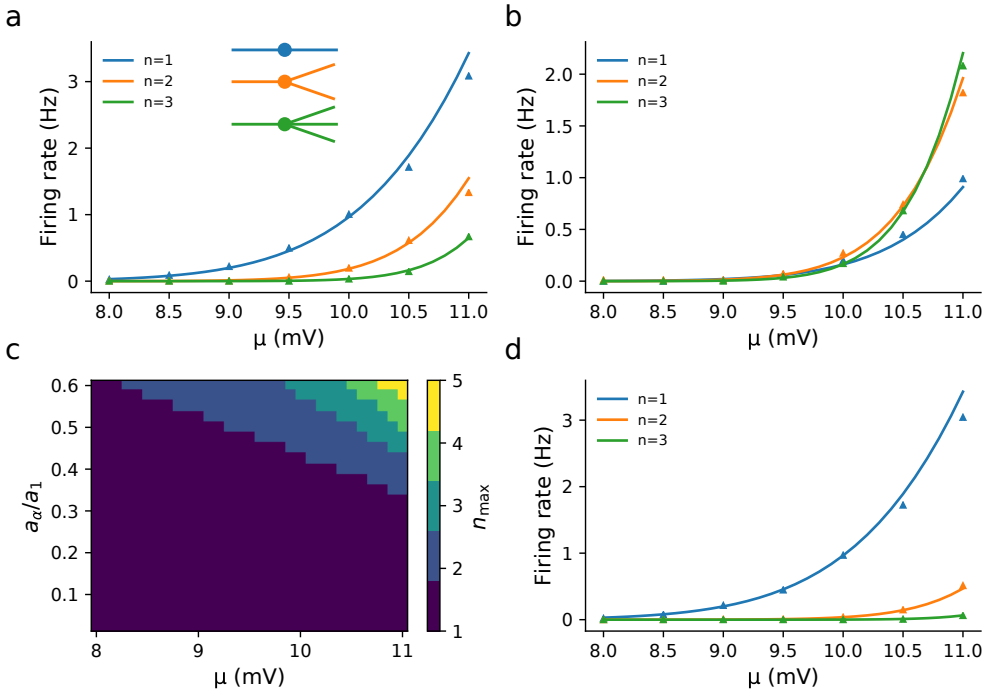

Fig 6. Increasing the number of synaptically driven dendrites can decrease the firing rate when the axon, of radius a_α is much thinner than the dendrite, radius a_1. The length constant for each neurite is proportional to the square root of the radius $\lambda_j \propto \sqrt{a_j}$. (a) $\lambda_\alpha = 100\mu$m, (b) $\lambda_\alpha = 150\mu$m, (c) The number $n_{\max}$ of dendrites that maximises firing increases with higher ratios of axon-to-dendrite radii a_α/a_1 and μ, (d) $\lambda_\alpha = 100\mu$m, $\lambda_1 = 200\mu$m for $n = 1$ and λ_1 is rescaled for larger n to keep the input conductance equal to the $n = 1$ case. Other parameters: $\lambda_1 = 200\mu$m (a-c), $\tau_1 = 10$ms, $\tau_\alpha = 11.7$ms (calculated from Eq (S39)), $\sigma_s = 3$mV, $v_{\text{th}} = 10$mV and $x_{\text{th}} = 30\mu$m down the axon.

additional complex impedance at the point where the axon and dendrites meet. This has the somatic boundary condition we gave earlier in Eq (15) and we recall that the subscript 0 denotes somatic quantities. For simplicity, and as neither section receives synaptic drive in our model, we will let the somatic time constant be the same as the axonal time constant, so $\tau_0 = \tau_\alpha$. Note that somatic drive can be straightforwardly added in this framework, as the variance contribution from the resultant fluctuations would add linearly: this would not qualitatively change the nature of the results we present here that focus on the effects of somatic filtering on transfer of dendritic stimulation to the trigger point in the axon. Note also that as $\rho_1 \to \infty$, the model without somatic drive converges to the dendrite and axon model with a nominal soma, allowing a clearer comparison between the two models.

For an electrically significant soma the integrand for the variance has the same form as before, Eq (S38), but $\tilde{f}$ now depends on the neurite dominance factor ρ,

$$\tilde{f}_{n0}(\omega) = \frac{G_{\lambda_1}\gamma_1}{G_0\gamma_0^2 + nG_{\lambda_1}\gamma_1 + G_{\lambda_\alpha}\gamma_\alpha} = \frac{\rho_1\gamma_1}{\gamma_0^2 + n\rho_1\gamma_1 + \rho_\alpha\gamma_\alpha}. \tag{32}$$

Thus for large n we should expect the variance in the axon to scale as $1/n$ as before, but for smaller n the somatic impedance $G_0\gamma_0^2$ gives some key differences. We repeated the simulations for the axon-dendrite model (Fig 6), first with a single dendrite and an

electrically significant soma by varying ρ_1, noting that with known λ_1 and λ_α, this also determines ρ_α, Eqs (S45, S46). Since the soma adds a conductance load G_0 to the cell the overall input resistance decreases. From Eq (32), we see that this will reduce $|\tilde{f}_{n0}(\omega)|$, for any number of dendrites which will lower both the mean and the variance. Fig 7a shows that the effect of a larger soma (lower ρ_1) lowers the firing rate.

Next, we investigated the effect an electrically significant soma has on axonal load, as seen previously for a nominal soma in Fig 5a. Like with the nominal soma case before, we calculated the firing rate at $x_{\rm th} = 0$ with an axon and electrically significant soma, $r_{\rm axon}$, and the firing rate of a dendrite with the same size soma without an axon, $r_{\rm no\ axon}$ (Fig 1a (vi)). For each somatic size, we adjusted σ_s so that the firing rate for a negligible axon, $a_\alpha/a_1 = 0$, the firing rate was fixed at 1Hz. This was done to account for the soma's effect on the firing rate we observed earlier and we are thus solely focusing on the effect of the axonal admittance load. As we increase $a_\alpha/a_1 = 0$ Fig 7b shows that $r_{\rm axon}/r_{\rm no\ axon}$ decreases more rapidly with increasing a_α/a_1 for larger ρ_1 (smaller soma). This means that, in comparison to Fig 5a, the axonal load had a lower relative effect on the firing rate in the presence of a soma. This is in line with what we should expect by looking at $\tilde{f}_{n0}$; lower ρ_1 increases the relative magnitude of $G_0\gamma_0^2$ in the denominator of $\tilde{f}_{n0}$ as compared with the axonal admittance term of $G_{\lambda_\alpha}\gamma_\alpha$.

Finally, we looked at how an electrically significant soma affects the dependence of the firing rate on the number of dendrites. By varying ρ_1 and the number of dendrites n, Fig 7c shows that the non-monotonic dependence of the firing rate on dendritic number n is robust in the presence of a soma. Fig 7d illustrates that the number of dendrites that maximises the firing rate is greater for lower ρ_1 and higher μ. We have discussed previously why the value of n that maximises firing increases with μ as the increase in mean from additional dendrites becomes more significant for the firing rate. Decreasing ρ_1 increases the value of n that maximises firing because the relative increase in conductance by adding another dendrite is smaller when the fixed somatic conductance is larger.

Discussion

This study demonstrated how the spatio-temporal fluctuation-driven firing of neurons with dendrites, soma and axon can be approximated using the upcrossing method of Rice [27]. Despite being reduced models of neuronal structures, they demonstrate considerable richness in behaviour beyond what point-like or compartmental models capture. For the one and two-dendrite models, the firing rate was shown to be independent of the electrotonic length constant; given that the length constant sets the range over which synaptic drive contributes to voltage fluctuations, this result is surprising. However, a dimensional argument extends this independence to any model in which semi-infinite neurites are joined at a point and share the same λ (any other properties without dimensions of length can be different in each neurite). The level-crossing approach provided a good approximation for the firing rate for these simple dendritic neuron models in the low-rate limit. Beyond this limit, simulations suggest that there is a universal functional form for the firing rate when parametrised by σ_v that is independent of both λ and the number of dendrites radiating from the nominal soma. This functional form, for coloured noise and in the white-noise limit, merits further mathematical analysis as it is distinct to that of the point-like integrate-and-fire model.

Extending the study to multiple dendrites, we showed that the firing rate depends non-monotonically on their number: adding more dendrites driven by fluctuating synaptic drive can, for a broad parameter range, decrease the fluctuation-driven firing rate. Dendritic structure has been previously shown to influence the firing rate for

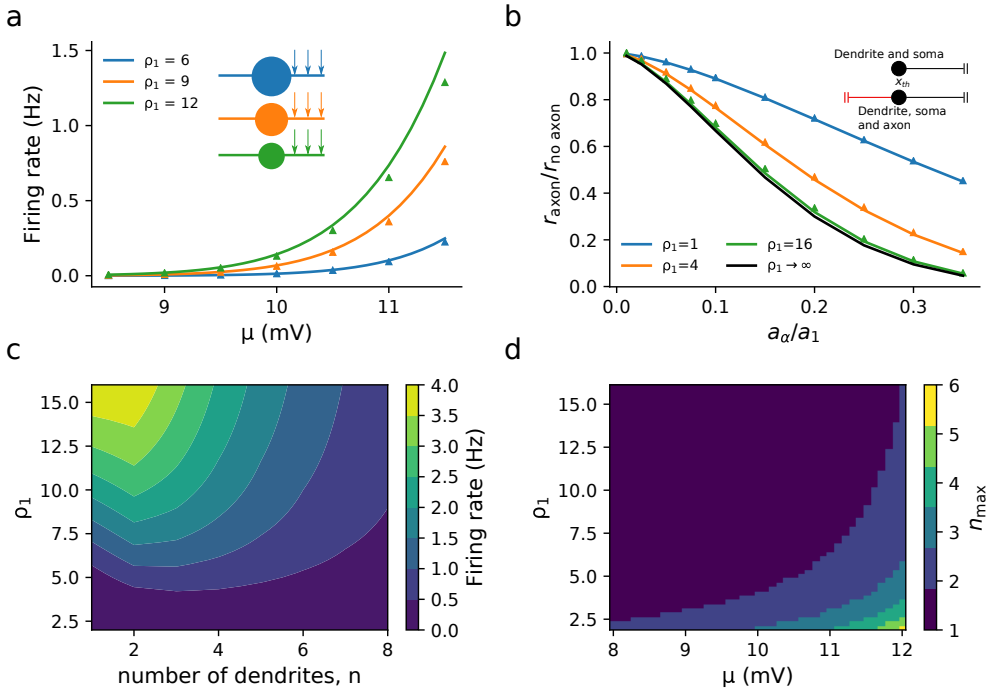

Fig 7. Effect of somatic impedance between a synaptically driven dendrite and axon with trigger point $x_{\text{th}}=30\mu$m for (a), (c) and (d) and $x_{\text{th}}=0\mu$m for (b). (a) The soma is characterised by the dendritic dominance factor ρ_1 (see main text) with large ρ_1 corresponding to a small somatic conductance. (b) A larger soma masks the effect of the axonal load on the firing rate, although this masking is negligible for smaller somata $\rho_1 = 16$. Fig 2a (black line) result is plotted for comparison. (c) Larger somata also reduce the firing rate in the case of n dendrites ($\mu=12$mV). (d) With larger μ, smaller ρ_1 (a larger soma) increases the number of dendrites for which the firing rate is maximal, $n_{\max}$. Other parameters: $\tau_1=10$ms, $\tau_\alpha=11.7$ms, $\lambda_1=200\mu$m, $\lambda_\alpha=100\mu$m (calculated from Eq (S39)), $\sigma_s=3$mV, $v_{\text{th}}=10$mV, ρ_α calculated from Eqs (S45) or (S46)

deterministic input [64,65]. However, apart from the work of Tuckwell [30–32], analytical studies of stochastic drive in extended neuron models have largely focussed on a single dendrite with drive typically applied at a single point [36,39] rather than distributed over the dendrite, or as a two-compartmental model [66]. This study demonstrates that in the low-rate regime, the upcrossing approximation allows for the analytical study of spatial models that need not be limited to a single dendrite nor with stochastic synaptic drive confined to a single point, but distributed as is the case *in vivo*.

Including axonal and somatic conductance loads demonstrated their significant effect on the firing rate - even relatively small axonal loads caused a marked reduction. Furthermore, the non-monotonic dependency of the firing rate on dendrite number was also shown to be affected by axonal radius and somatic size, demonstrating that the upcrossing method can be used to examine how structural differences in properties affect the firing rate of complex, composite, spatial neuron models.

The advantage of the level-crossing approach is it can be straightforwardly extended to include a great variety of additional biophysical properties affecting neuronal integration of spatio-temporal synaptic drive. An example of this for pyramidal neurons would be the inclusion of non-passive effects arising from voltage-gated currents such as I_h [67]. The only requirement for the upcrossing approximation is the derivation of the

voltage mean, variance and rate-of-change variance at the point that action potentials are triggered. For many scenarios, particularly in the high-conductance state, the spatio-temporal response can be approximated as quasi-linear, allowing the voltage moments to be calculated via Green's functions using existing theoretical machinery, such as sum-over-trips on neurons [68–70]. The approach can also be extended to examine the dynamic firing-rate response to weakly modulated drive. This has already been done for point-neurons using the upcrossing method [29, 71, 72] and would only necessitate calculating the linear-response of voltage moments in the non-threshold case.

In summary, the extension of the upcrossing approach to spatially structured neuron models provides an analytical in-road for future studies of the firing properties of extended neuron models driven by spatio-temporal stochastic synaptic drive.

References

1. Larkman AU. Dendritic Morphology of Pyramidal Neurones of the Visual Cortex of the Rat: 111. Spine Distributions. The Journal of Comparative Neurology. 1991;306:332–343. doi:10.1002/cne.903060209.

2. Markram H, Toledo-Rodriguez M, Wang Y, Gupta A, Silberberg G, Wu C. Interneurons of the neocortical inhibitory system. Nature Reviews Neuroscience. 2004;5(10):793–807.

3. Larkman A, Mason A. Correlations between morphology and electrophysiology of pyramidal neurons in slices of rat visual cortex. I. Establishment of cell classes. The Journal of Neuroscience. 1990;10(5):1407–1414. doi:10.1523/JNEUROSCI.10-05-01407.1990.

4. Ramaswamy S, Markram H. Anatomy and physiology of the thick-tufted layer 5 pyramidal neuron. Frontiers in Cellular Neuroscience. 2015;9. doi:10.3389/fncel.2015.00233.

5. Holt GR, Softky WR, Koch C, Douglas RJ. Comparison of discharge variability in vitro and in vivo in cat visual cortex neurons. Journal of Neurophysiology. 1996;75(5):1806–1814.

6. Barth AL, Poulet JFA. Experimental evidence for sparse firing in the neocortex. Trends in Neurosciences. 2012;35(6):345–355. doi:10.1016/j.tins.2012.03.008.

7. Silberberg G, Bethge M, Markram H, Pawelzik K, Tsodyks M. Dynamics of Population Rate Codes in Ensembles of Neocortical Neurons. Journal of Neurophysiology. 2004;91(2):704–709. doi:10.1152/jn.00415.2003.

8. London M, Roth A, Beeren L, Häusser M, Latham PE. Sensitivity to perturbations in vivo implies high noise and suggests rate coding in cortex. Nature. 2010;466(7302):123–127. doi:10.1038/nature09086.

9. Sengupta B, Faisal AA, Laughlin SB, Niven JE. The Effect of Cell Size and Channel Density on Neuronal Information Encoding and Energy Efficiency. Journal of Cerebral Blood Flow & Metabolism. 2013;33(9):1465–1473. doi:10.1038/jcbfm.2013.103.

10. Bindman LJ, Meyer T, Prince CA. Comparison of the electrical properties of neocortical neurones in slices in vitro and in the anaesthetized rat. Experimental Brain Research. 1988;69(3). doi:10.1007/BF00247303.

11. Holmes WR, Woody CD. Effects of uniform and non-uniform synaptic activation-distributions on the cable properties of modeled cortical pyramidal neurons. Brain Research. 1989;505(1):12–22. doi:10.1016/0006-8993(89)90110-8.

12. Paré D, Shink E, Gaudreau H, Destexhe A, Lang EJ. Impact of Spontaneous Synaptic Activity on the Resting Properties of Cat Neocortical Pyramidal Neurons In Vivo. Journal of Neurophysiology. 1998;79(3):1450–1460. doi:10.1152/jn.1998.79.3.1450.

13. Köndgen H, Geisler C, Fusi S, Wang XJ, Lüscher HR, Giugliano M. The dynamical response properties of neocortical neurons to temporally modulated noisy inputs in vitro. Cerebral Cortex. 2008;18(9):2086–2097.

14. Doose J, Doron G, Brecht M, Lindner B. Noisy Juxtacellular Stimulation In Vivo Leads to Reliable Spiking and Reveals High-Frequency Coding in Single Neurons. Journal of Neuroscience. 2016;36(43):11120–11132. doi:10.1523/JNEUROSCI.0787-16.2016.

15. Stein RB. A Theoretical Analysis of Neuronal Variability. Biophys J. 1965;5(2):173–194. doi:10.1016/S0006-3495(65)86709-1.

16. Knight BW. Dynamics of Encoding in a Population of Neurons. J Gen Physiol. 1972;59(6):734–766. doi:10.1085/jgp.59.6.734.

17. Burkitt AN. A review of the integrate-and-fire neuron model: I. Homogeneous synaptic input. Biological Cybernetics. 2006;95(1):1–19. doi:10.1007/s00422-006-0068-6.

18. Burkitt AN. A review of the integrate-and-fire neuron model: II. Inhomogeneous synaptic input and network properties. Biological Cybernetics. 2006;95(2):97–112. doi:10.1007/s00422-006-0082-8.

19. Brunel N, Hakim V, Richardson MJ. Single neuron dynamics and computation. Current Opinion in Neurobiology. 2014;25:149–155. doi:10.1016/j.conb.2014.01.005.

20. Brunel N, Hakim V. Fast global oscillations in networks of integrate-and-fire neurons with low firing rates. Neural Computation. 1999;11(7):1621–1671.

21. Lindner B, Schimansky-Geier L. Transmission of Noise Coded versus Additive Signals through a Neuronal Ensemble. Physical Review Letters. 2001;86(14):2934–2937. doi:10.1103/PhysRevLett.86.2934.

22. Fourcaud-Trocmé N, Hansel D, Van Vreeswijk C, Brunel N. How spike generation mechanisms determine the neuronal response to fluctuating inputs. Journal of Neuroscience. 2003;23(37):11628–11640.

23. Richardson MJE. Firing-rate response of linear and nonlinear integrate-and-fire neurons to modulated current-based and conductance-based synaptic drive. Physical Review E. 2007;76(2):021919.

24. Brunel N, Sergi S. Firing frequency of leaky integrate-and-fire neurons with synaptic current dynamics. Journal of Theoretical Biology. 1998;195(1):87–95. doi:10.1006/jtbi.1998.0782.

25. Brunel N, Chance FS, Fourcaud N, Abbott LF. Effects of synaptic noise and filtering on the frequency response of spiking neurons. Physical Review Letters. 2001;86(10):2186–2189. doi:10.1103/PhysRevLett.86.2186.

26. Alijani AK, Richardson MJE. Rate response of neurons subject to fast or frozen noise: From stochastic and homogeneous to deterministic and heterogeneous populations. Physical Review E. 2011;84(1). doi:10.1103/PhysRevE.84.011919.

27. Rice SO. Mathematical analysis of random noise Part III. Bell Sys Tech J. 1945;24(1):46–156. doi:10.1002/j.1538-7305.1944.tb00874.x.

28. Tchumatchenko T, Malyshev A, Geisel T, Volgushev M, Wolf F. Correlations and synchrony in threshold neuron models. Physical Review Letters. 2010;104(5):058102.

29. Badel L. Firing statistics and correlations in spiking neurons: A level-crossing approach. Physical Review E. 2011;84(4):041919. doi:10.1103/PhysRevE.84.041919.

30. Tuckwell HC, Walsh JB. Random currents through nerve membranes - I. Uniform poisson or white noise current in one-dimensional cables. Biol Cybern. 1983;49(2):99–110. doi:10.1007/BF00320390.

31. Tuckwell HC. Spatial neuron model with two-parameter Ornstein-Uhlenbeck input current. Physica A: Statistical Mechanics and its Applications. 2006;368(2):495–510. doi:10.1016/j.physa.2005.12.022.

32. Tuckwell HC. Analytical and simulation results for the stochastic spatial FitzHugh-Nagumo model neuron. Neural Computation. 2008;20(12):3003–3033.

33. Rudolph M, Destexhe A. A Fast-Conducting, Stochastic Integrative Mode for Neocortical Neurons *In Vivo*. Journal of Neuroscience. 2003;23(6):2466–2476. doi:10.1523/JNEUROSCI.23-06-02466.2003.

34. Zhang C, Hofmann D, Neef A, Wolf F. Ultrafast population coding and axo-somatic compartmentalization. arXiv preprint arXiv:180700509. 2018;.

35. Pettersen KH, Lindn H, Tetzlaff T, Einevoll GT. Power Laws from Linear Neuronal Cable Theory: Power Spectral Densities of the Soma Potential, Soma Membrane Current and Single-Neuron Contribution to the EEG. PLOS Computational Biology. 2014;10(11):e1003928.

36. Aspart F, Ladenbauer J, Obermayer K. Extending Integrate-and-Fire Model Neurons to Account for the Effects of Weak Electric Fields and Input Filtering Mediated by the Dendrite. PLOS Computational Biology. 2016;12(11):e1005206. doi:10.1371/journal.pcbi.1005206.

37. Ladenbauer J, Obermayer K. Weak electric fields promote resonance in neuronal spiking activity: Analytical results from two-compartment cell and network models. PLOS Computational Biology. 2019;15(4):e1006974. doi:10.1371/journal.pcbi.1006974.

38. Kole MHP, Stuart GJ. Signal Processing in the Axon Initial Segment. Neuron. 2012;73(2):235–247. doi:10.1016/j.neuron.2012.01.007.

39. Eyal G, Mansvelder HD, de Kock CP, Segev I. Dendrites impact the encoding capabilities of the axon. Journal of Neuroscience. 2014;34(24):8063–8071.

40. Spontaneous Action Potentials and Neural Coding in Unmyelinated Axons. Neural Computation;27(4).

41. Hamada MS, Goethals S, Vries SID, Brette R, Kole MHP. Covariation of axon initial segment location and dendritic tree normalizes the somatic action potential. Proceedings of the National Academy of Sciences. 2016;113(51). doi:10.1073/pnas.1607548113.

42. Kole MH, Brette R. The electrical significance of axon location diversity. Current Opinion in Neurobiology. 2018;51:52–59. doi:10.1016/j.conb.2018.02.016.

43. Packer AM, Roska B, Häusser M. Targeting neurons and photons for optogenetics. Nature Neuroscience. 2013;16(7):805.

44. Malyshev A, Goz R, LoTurco JJ, Volgushev M. Advantages and limitations of the use of optogenetic approach in studying fast-scale spike encoding. PLOS One. 2015;10(4):e0122286.

45. Ferrarese L, et al. Dendrite-Specific Amplification of Weak Synaptic Input during Network Activity In Vivo. Cell Reports. 2018;24(13):3455–3465.e5. doi:10.1016/j.celrep.2018.08.088.

46. Koch K, Fuster J. Unit activity in monkey parietal cortex related to haptic perception and temporary memory. Experimental Brain Research. 1989;76(2):292–306.

47. Hromádka T, DeWeese MR, Zador AM. Sparse Representation of Sounds in the Unanesthetized Auditory Cortex. PLOS Biology. 2008;6(1):e16. doi:10.1371/journal.pbio.0060016.

48. Buzsáki G, Mizuseki K. The log-dynamic brain: how skewed distributions affect network operations. Nature Reviews Neuroscience. 2014;15(4):264–278. doi:10.1038/nrn3687.

49. Buzsáki G, Kandel A. Somadendritic Backpropagation of Action Potentials in Cortical Pyramidal Cells of the Awake Rat. Journal of Neurophysiology. 1998;79(3):1587–1591. doi:10.1152/jn.1998.79.3.1587.

50. London M, Häusser M. Dendritic computation. Annual Reviews of Neuroscience. 2005;28:503–532.

51. Hill DN, Varga Z, Jia H, Sakmann B, Konnerth A. Multibranch activity in basal and tuft dendrites during firing of layer 5 cortical neurons in vivo. Proceedings of the National Academy of Sciences. 2013;110(33):13618–13623. doi:10.1073/pnas.1312599110.

52. Rall W. Core conductor theory and cable properties of neurons. In: Comprehensive Physiology. Wiley Online Library; 2011. p. 39–97.

53. Bezanson J, Edelman A, Karpinski S, Shah VB. Julia: A fresh approach to numerical computing. SIAM review. 2017;59(1):65–98.

54. Code to be supplied as supplementary information in published paper.

55. Yang L, Alouini MS. Level crossing rate over multiple independent random processes: An extension of the applicability of the Rice formula. IEEE Transactions on Wireless Communications. 2007;6(12):4280–4284.

56. Baxevani A, Podgórski K, Rychlik I. Velocities for moving random surfaces. Probabilistic Engineering Mechanics. 2003;18(3):251–271.

57. Schoepe W. Fluctuations and Stability of Superfluid Turbulence at mK Temperatures. Physical Review Letters. 2004;92(9):095301. doi:10.1103/PhysRevLett.92.095301.

58. Shahbazi F, Sobhanian S, Tabar MRR, Khorram S, Frootan G, Zahed H. Level crossing analysis of growing surfaces. Journal of Physics A. 2003;36(10):2517.

59. Lánský P, Rodriguez R. Two-compartment stochastic model of a neuron. Physica D. 1999;132(1-2):267–286. doi:10.1016/S0167-2789(99)00034-2.

60. Palmer LM, Stuart GJ. Site of action potential initiation in layer 5 pyramidal neurons. Journal of Neuroscience. 2006;26(6):1854–1863. doi:10.1523/JNEUROSCI.4812-05.2006.

61. Shu Y, Duque A, Yu Y, Haider B, McCormick DA. Properties of action-potential initiation in neocortical pyramidal cells: evidence from whole cell axon recordings. Journal of Neurophysiology. 2007;97(1):746–60. doi:10.1152/jn.00922.2006.

62. Kole MHP, et al. Action potential generation requires a high sodium channel density in the axon initial segment. Nature Neuroscience. 2008;11(2):178–186. doi:10.1038/nn2040.

63. Höfflin F, et al. Heterogeneity of the Axon Initial Segment in Interneurons and Pyramidal Cells of Rodent Visual Cortex. Frontiers in Cellular Neuroscience. 2017;11:332. doi:10.3389/fncel.2017.00332.

64. Mainen ZF, Sejnowski TJ. Influence of dendritic structure on firing pattern in model neocortical neurons. Nature. 1996;382(July):1–4.

65. van Ooyen A, Duijnhouwer J, Remme MWH, van Pelt J. The effect of dendritic topology ion firing patterns in model neurons. Neurocomputing. 2002;13:311–325.

66. Ostojic S, et al. Neuronal morphology generates high-frequency firing resonance. Journal of Neuroscience. 2015;35(18):7056–7068.

67. Puelma Touzel M, Wolf F. Complete Firing-Rate Response of Neurons with Complex Intrinsic Dynamics. PLOS Computational Biology. 2015;11(12):e1004636. doi:10.1371/journal.pcbi.1004636.

68. Abbott LF, Farhi E, Gutmann S. The path integral for dendritic trees. Biological Cybernetics. 1991;66(1):49–60.

69. Coombes S, Timofeeva Y, Svensson CM, Lord GJ, Josić K, Cox SJ, et al. Branching dendrites with resonant membrane: a "sum-over-trips" approach. Biological Cybernetics. 2007;97(2):137–149. doi:10.1007/s00422-007-0161-5.

70. Yihe L, Timofeeva Y. Response functions for electrically coupled neuronal network: a method of local point matching and its applications. Biological Cybernetics. 2016;110(2-3):117–133. doi:10.1007/s00422-016-0681-y.

71. Tchumatchenko T, Wolf F. Representation of Dynamical Stimuli in Populations of Threshold Neurons. PLOS Computational Biology. 2011;7(10):e1002239. doi:10.1371/journal.pcbi.1002239.

72. Tchumatchenko T, Clopath C. Oscillations emerging from noise-driven steady state in networks with electrical synapses and subthreshold resonance. Nature Communications. 2014;5:5512.

73. Tuckwell HC. Time-dependent cable theory for nerve cylinders and dendritic trees. In: Introduction to theoretical neurobiology: volume 1, linear cable theory and dendritic structure. Cambridge University Press; 1988. p. 180–233.

74. Manwani A, Koch C. Detecting and Estimating Signals in Noisy Cable Structures, I: Neuronal Noise Sources. Neural Computation. 1999;11(8):1797–1829.

Appendix

Green's functions

For notational simplicity we choose to measure distance in each neurite in terms of the length constant so $x_k/\lambda_k \to x_k$ and $y_k/\lambda_k \to y_k$. In the Fourier domain, the Green's function $\tilde{\mathcal{G}}_{jk}(x_j, y_k; \omega)$ denotes the response at x_j in neurite j to an input in neurite k at y_k. The voltage due to an input in the Fourier domain $\tilde{I}$ is given in terms of the double integral

$$v(x,t) = \frac{1}{2\pi}\int_{-\infty}^{\infty} e^{i\omega t}\mathrm{d}\omega \int_0^{\infty} \tilde{\mathcal{G}}(x,y;\omega)\tilde{I}(y;\omega)\mathrm{d}y. \tag{S1}$$

The Green's function in the Fourier domain for Eq (18) satisfies the equation

$$\gamma_j^2 \tilde{\mathcal{G}}_{jk} = \frac{\partial^2 \tilde{\mathcal{G}}_{jk}}{\partial x_j^2} + \delta_{jk}\delta(x_j - y_k), \tag{S2}$$

where δ_{jk} is the Kronecker delta function. Eq (S2) has the general solution

$$\tilde{\mathcal{G}}_{jk}(x_j, y_k; \omega) = c_1 e^{-x_j\gamma_j} + c_2 e^{x_j\gamma_j} - \delta_{jk}\frac{\theta(x_j - y_k)}{2\gamma_j}[e^{(x_j - y_k)\gamma_j} - e^{-(x_j - y_k)\gamma_j}], \tag{S3}$$

where the Heaviside step function $\theta(.)$ is only relevant if the input neurite and output neurite are the same. As the Green's function inherits the boundary conditions of the system it describes, we apply a model's boundary conditions to Eq (S3) to obtain the specific solution. Green's functions for each of the cases studied in this paper are given later in this appendix. For an infinite dendrite, the Green's function has the well-known form [73]

$$\tilde{\mathcal{G}}_{\infty}(x - y; \omega) = \frac{e^{-|x-y|\gamma}}{2\gamma}, \tag{S4}$$

where $\gamma_j = \sqrt{1 + i\omega\tau_j}$. For multiple neurites and a soma, one can build more complex Green's functions from a generalisation of Eq (S4) using the sum-over-trips formalism [68, 69]

$$\tilde{\mathcal{G}}_{\infty}(x_j \pm y_k, \omega) = \begin{cases} e^{-|x_j - y_k|\gamma_k}/(2\gamma_k), & j = k \\ e^{-(x_j\gamma_j + y_k\gamma_k)}/(2\gamma_k), & j \neq k \end{cases}. \tag{S5}$$

The only additional calculation that needs to be made is the segment factor $\tilde{f}(\omega)$. This quantity is the ratio of the admittance of the input neurite Y_k (with $k{=}\alpha$ indicating the axon), to the total admittance of all neurites which radiate from the same node. For n dendrites radiating from a node with a soma this is

$$\tilde{f}(\omega) = \frac{Y_k}{Y_\alpha + Y_0 + \sum_{j=1}^{n} Y_j}. \tag{S6}$$

For each neurite, the admittance is given by

$$Y_j = 2\pi g_j a_j \lambda_j \gamma_j, \tag{S7}$$

where g_j is the total membrane conductance (including tonic synaptic conductance) while for a soma with membrane conductance G_0, the admittance is

$$Y_0 = G_0 \gamma_0^2. \tag{S8}$$

If there is only a single path from x_j to y_k and $j \neq k$, then the Green's function is given by Eq (S23)

$$\tilde{\mathcal{G}}_{jk}(x_j, y_k; \omega) = 2\tilde{f}(\omega)\tilde{\mathcal{G}}_\infty(x_j + y_k; \omega). \tag{S9}$$

Calculation of moments

The input I to each neurite has a deterministic and stochastic component, which in the Fourier domain are

$$\tilde{I}_k = 2\pi\delta(\omega)\mu_k + \tilde{s}_k, \quad \tilde{s}_k = \frac{2\sigma_s\sqrt{\tau_s}\tilde{\xi}(x_k;\omega)}{1 + i\omega\tau_s}, \tag{S10}$$

where we have again removed the units from distance. Since the system is linear, this means that the voltage will have a mean and fluctuating component

$$v(x,t) = \langle v(x)\rangle + v_F(x,t). \tag{S11}$$

Substituting $\tilde{I}$ into Eq (S1) and taking the expectation, the mean in neurite j due to input in k is

$$\langle v_{jk}(x_j)\rangle = \mu_k \int_0^\infty \tilde{\mathcal{G}}_{jk}(x_j, y_k; 0)\mathrm{d}y_k \tag{S12}$$

while the fluctuating component is

$$v_{Fjk}(x_j,t) = \frac{\sigma_s\sqrt{\tau_s}}{\pi}\int_{-\infty}^\infty e^{i\omega t}\mathrm{d}\omega \int_0^\infty \frac{\tilde{\mathcal{G}}_{jk}(x_j, y_k;\omega)}{1+i\omega\tau_s}\tilde{\xi}(y_k;\omega)\mathrm{d}y_k. \tag{S13}$$

Thus the variance contribution from neurite k is obtained by squaring v_{Fjk} and taking the expectation, noting that $\langle\tilde{\xi}_j(y_j,\omega)\tilde{\xi}_k(y_k',-\omega')\rangle = 2\pi\delta_{jk}\delta(y-y')\delta(\omega-\omega')$,

$$\sigma^2_{vjk}(x_j) = \frac{2\sigma_s^2\tau_s}{\pi}\int_{-\infty}^\infty \mathrm{d}\omega \int_0^\infty \frac{|\tilde{\mathcal{G}}_{jk}(x_j, y_k;\omega)|^2}{1+\omega^2\tau_s^2}\mathrm{d}y_k, \tag{S14}$$

and similarly the variance of the voltage time derivative is found by multiplying the integrand of Eq (S14) by ω^2

$$\sigma^2_{\dot{v}jk}(x_j) = \frac{2\sigma_s^2\tau_s}{\pi}\int_{-\infty}^\infty \mathrm{d}\omega \int_0^\infty \frac{\omega^2|\tilde{\mathcal{G}}_{jk}(x_j, y_k;\omega)|^2}{1+\omega^2\tau_s^2}\mathrm{d}y_k. \tag{S15}$$

This approach is equivalent to that found in [74], where the integrand of Eqs (S14, S15) is proportional to the power spectral density of the voltage. With these integrals for the second moments, the definition $z_j = \gamma_j + \gamma_j^*$ is useful for keeping the algebra compact.

For n dendrites with synaptic input, the response in the axon is simply the linear sum from each dendrite,

$$\langle v_\alpha(x_\alpha)\rangle = \sum_{k=1}^n \langle v_{\alpha k}(x_\alpha)\rangle, \quad v_{F\alpha}(x_\alpha) = \sum_{k=1}^n v_{F\alpha k}(x_\alpha), \tag{S16}$$

and since the stochastic drive between dendrites is uncorrelated, the second moment contributions from each dendrite also sum linearly,

$$\sigma_v^2(x_\alpha) = \sum_{k=1}^{n} \sigma_{v_\alpha k}^2(x_\alpha), \quad \sigma_{\dot{v}}^2(x_\alpha) = \sum_{k=1}^{n} \sigma_{\dot{v}_\alpha k}^2(x_\alpha). \tag{S17}$$

For dendrites with identical properties and drive, this means we can multiply Eqs (S14, S15) by n to obtain the total second moments.

In all the cases given, $\langle v \rangle$ is easily analytically calculable. For the infinite dendrite $\langle v \rangle = \mu$, while the resting potential in the axon for n dendrites is

$$\langle v(x_\alpha) \rangle = \tfrac{1}{2} n\mu e^{-x_\alpha} \tilde{f}_n(0) \tag{S18}$$

and the addition of a soma changes this to

$$\langle v(x_\alpha) \rangle = \tfrac{1}{2} n\mu e^{-x_\alpha} \tilde{f}_{n0}(0). \tag{S19}$$

For many simple cases - such as the sealed dendrite, one-dendrite, and two-dendrite models - closed-form expressions for the second moments are attainable. For all cases with an axon and/or soma with different membrane properties to the dendrite, the ω-integral can be calculated numerically or approximated in a limit of interest. However, given the n in the denominator of $\tilde{f}_n$ and $\tilde{f}_{n0}$, we expect from Eqs (S14, S15) that the second moments scale as $\sim 1/n$ for large n.

Derivation of Green's functions

Closed dendrite

Given the zero-current boundary conditions at the ends $x = [0, l]$

$$\left.\frac{\partial v}{\partial x}\right|_{x=0} = 0 = \left.\frac{\partial v}{\partial x}\right|_{x=l}, \tag{S20}$$

we can solve the Green's function differential equation, Eq(S2), to obtain [73]

$$\tilde{\mathcal{G}}(x, y; \omega) = \frac{\cosh[(l - |x - y|)\gamma] + \cosh[(l - |x + y|)\gamma]}{2\gamma \sinh(l\gamma)}. \tag{S21}$$

Dendrite and axon

Using the sum-over-trips method, $\tilde{\mathcal{G}}_{jk}$ is given by the sum of infinite Green's functions of each path which traces back from output position x_j to input position y_k. If a given path has length l_{trip}, then we represent this sum as [68, 69]

$$\tilde{\mathcal{G}}_{jk}(x_j, y_k; \omega) = \sum_{\text{trips}} A_{\text{trip}}(\omega) \tilde{\mathcal{G}}_\infty(l_{\text{trip}}; \omega), \tag{S22}$$

where A_{trip} is the trip coefficient that depends on the intersections between cables that a trip must path through. Since the neurites we consider are semi-infinite, there is only a single trip for a path from the axon to the input dendrite (however, the sum-over-trips approach provides a method for straightforward generalisation to dendrites with closed ends). The only trip coefficient required is that for transmission through a node which is given by $A_{\text{trip}} = 2\tilde{f}(\omega)$ [69]. Therefore, the Green's function from the dendrite $k=1$ to the axon, $j=\alpha$, is given by

$$\tilde{\mathcal{G}}_{\alpha 1}(x_\alpha, y_1; \omega) = 2\tilde{f}(\omega) \tilde{\mathcal{G}}_\infty(x_\alpha + y_1; \omega), \tag{S23}$$

which upon substitution of $\tilde{f}$ and $\tilde{\mathcal{G}}_\infty$ yields

$$\tilde{\mathcal{G}}_{\alpha 1}(x_\alpha, y_1; \omega) = \frac{g_1^2 \lambda_1^3 \gamma_1}{\gamma_1 (g_1^2 \lambda_1^3 \gamma_1 + g_\alpha^2 \lambda_\alpha^3 \gamma_\alpha)} e^{-(x_\alpha \gamma_\alpha + y_1 \gamma_1)}. \tag{S24}$$

Multiple dendrites and axon

When there are n dendrites, the segment factor becomes

$$\tilde{f}_n(\omega) = \frac{g_1^2\lambda_1^3\gamma_1}{ng_1^2\lambda_1^3\gamma_1 + g_\alpha^2\lambda_\alpha^3\gamma_\alpha}, \tag{S25}$$

and hence the Green's function for the axonal response is

$$\tilde{\mathcal{G}}_{\alpha 1}(x_\alpha, y_1; \omega) = \frac{g_1^2\lambda_1^3\gamma_1}{\gamma_1(ng_1^2\lambda_1^3\gamma_1 + g_\alpha^2\lambda_\alpha^3\gamma_\alpha)} e^{-(x_\alpha\gamma_\alpha + y_1\gamma_1)}. \tag{S26}$$

Since all dendrites have the same properties for this model, we can then claim that $\tilde{\mathcal{G}}_{\alpha 1} = \tilde{\mathcal{G}}_{\alpha 2} = ... = \tilde{\mathcal{G}}_{\alpha n}$.

Dendrites, soma and axon

For an electrically significant soma, the segment factor is now

$$\tilde{f}_{n0}(\omega) = \frac{\rho_1\gamma_1}{\gamma_0^2 + n\rho_1\gamma_1 + \rho_\alpha\gamma_\alpha}, \tag{S27}$$

hence the Green's function is

$$\tilde{\mathcal{G}}_{\alpha 1}(x_\alpha, y_1; \omega) = \frac{\rho_1\gamma_1}{\gamma_1(\gamma_0^2 + n\rho_1\gamma_1 + \rho_\alpha\gamma_\alpha)} e^{-(x_\alpha\gamma_\alpha + y_1\gamma_1)}. \tag{S28}$$

Derivation of second moments

With an additive input in the Fourier domain $\tilde{I}(y;\omega)$, the voltage in the Fourier domain is given by

$$\tilde{v}(x,\omega) = \int_0^\infty \tilde{\mathcal{G}}(x,y;\omega)\tilde{I}(y;\omega)\mathrm{d}y, \tag{S29}$$

and after taking the inverse Fourier transform we obtain Eq (S1). While there are other methods for obtaining second moments that may be more convenient for the models which provide closed-form solutions (such as a Green's functions in time [30] or Fourier series decomposition [30–32]) the method we present here extends most easily to arbitrary neuronal structures. For clarity of explanation, we derive the two-dendrite model first.

Two-dendrite model

For the two-dendrite model $|\tilde{\mathcal{G}}|^2$ is given by

$$|\tilde{\mathcal{G}}(x,y;\omega)|^2 = \frac{e^{-xz}}{4|\gamma|^2} \tag{S30}$$

which we can readily integrate with respect to y after substituting into Eq (S14) to receive

$$\sigma_v^2 = \frac{\sigma_s^2\tau_s}{\pi}\int_{-\infty}^{\infty} \frac{\mathrm{d}\omega}{z|\gamma|^2(1+\omega^2\tau_s^2)}. \tag{S31}$$

Using the substitution $\omega\tau_v = 2q\sqrt{q^2-1}$ and splitting into partial fractions this integral becomes

$$\sigma_v^2 = \frac{2\sigma_s^2\tau_s}{\pi\tau_v}\left\{\int_0^\infty \frac{\mathrm{d}q}{q^2+1} - \int_0^\infty \frac{4\tau_s^2q^2\mathrm{d}q}{\tau_v^2 + 4\tau_s^2q^2(q^2+1)}\right\}, \tag{S32}$$

which can be resolved to give Eq (24).

One-dendrite model

Defining $iu = \gamma - \gamma^*$ we find

$$|\tilde{\mathcal{G}}(x,y;\omega)|^2 = \begin{cases} e^{-xz}(e^{yz}+e^{-yz}+e^{iyu}+e^{-iyu})/(4|\gamma|^2), & y<x \\ e^{-yz}(e^{xz}+e^{-xz}+e^{iyu}+e^{-iyu})/(4|\gamma|^2), & y>x \end{cases}, \tag{S33}$$

which integrates with respect to y, giving

$$\sigma_v^2 = \frac{\sigma_s^2\tau_s}{\pi}\int_{-\infty}^{\infty}\frac{\mathrm{d}\omega}{|\gamma|^2(1+\omega^2\tau_s^2)}\left[\frac{1}{z}+e^{-xz}\frac{\sin(xu)}{u}+e^{-xz}\frac{\cos(xu)}{z}\right]. \tag{S34}$$

We can see that at $x=0$ and as $x\to\infty$ the variance is double and equal to the two-dendrite variance, respectively. For general x we can change the integration variable in a similar manner to the two-dendrite model to obtain the desired result.

Closed dendrite

With the closed dendrite, $|\tilde{\mathcal{G}}|^2$ is more lengthy

$$\begin{aligned} |\tilde{\mathcal{G}}(x,y;\omega)|^2 &= \{\tfrac{1}{2}\cosh[(l-x+y)z]+\tfrac{1}{2}\cos[(l-x+y)u] \\ &+\tfrac{1}{2}\cosh[(l-x-y)z]+\tfrac{1}{2}\cos[(l-x-y)u] \\ &+\cosh[(l-x)z]\cos(yu)+\cosh(yz)\cos[(l-x)u]\}/D, \quad y<x \qquad \text{(S35)} \\ &= \{\tfrac{1}{2}\cosh[(l+x-y)z]+\tfrac{1}{2}\cos[(l+x-y)u] \\ &+\tfrac{1}{2}\cosh[(l-x-y)z]+\tfrac{1}{2}\cos[(l-x-y)u] \\ &+\cosh[(l-y)z]\cos(xu)+\cosh(xz)\cos[(l-y)u]\}/D, \quad y>x \qquad \text{(S36)} \end{aligned}$$

where $D = 2|\gamma|^2[\cosh(lz)-\sin(lu)]$; however, we can see that all the functions involved will integrate with respect to y.

Dendrite and axon

For the dendrite and axon, we will leave $|\tilde{\mathcal{G}}|^2$ in terms of the segment factor to show how this approach extends to multiple dendrites and the addition of a soma

$$|\tilde{\mathcal{G}}_{\alpha 1}(x_\alpha,y_1;\omega)|^2 = \frac{|\tilde{f}_1(\omega)|^2}{|\gamma_1|^2}e^{-(x_\alpha z_\alpha+y_1 z_1)}. \tag{S37}$$

Integrating with respect to y gives,

$$\sigma_v^2(x_\alpha) = \frac{2\sigma_s^2\tau_s}{\pi}\int_{-\infty}^{\infty}\frac{|\tilde{f}_1(\omega)|^2 e^{-x_\alpha z_\alpha}}{z_1|\gamma_1|^2(1+\omega^2\tau_s^2)}\mathrm{d}\omega, \tag{S38}$$

which generalises to n dendrites or the addition of a soma by replacing $|\tilde{f}_1|^2$ with $|\tilde{f}_n|^2$ or $|\tilde{f}_{n0}(\omega)|^2$ respectively.

Calculation of axonal parameters

Assuming that the following parameters have the same value in the dendrite and axon: E_L, g_L and c_m, we can express the axonal parameters in terms of the dendritic ones. Since there is no synaptic drive in the axon, $g_\alpha = g_L$, while in the dendrite $g_1 = g_L + \langle g_s\rangle$. We denote the ratio between the membrane time constants as ϵ, which given constant c_m is

$$\epsilon = \frac{\tau_\alpha}{\tau_1} = \frac{g_L+\langle g_s\rangle}{g_L}. \tag{S39}$$

Recalling our definitions of E and μ in the dendrite as,

$$E = \frac{E_L g_L + E_s \langle g_s \rangle}{g_L + \langle g_s \rangle}, \quad \mu = E - E_L, \tag{S40}$$

we can rearrange to find an expression for ϵ in terms of potentials alone,

$$\epsilon = \frac{E_L - E_s}{E_L + \mu - E_s}. \tag{S41}$$

Hence we can calculate τ_α in terms of τ_1 given μ, E_L and E_s. For $E_L = -70\text{mV}$, $E_s = 0\text{mV}$ and $\mu = 10\text{mV}$ this results in $\epsilon = 7/6$.

When a_α and a_1 are fixed - as in Figs 5, 6c, and 7b - we can calculated λ_α in terms of a given λ_1. Recalling the definition of the length constant from Eq (7) and making the reasonable assumption that the axial resistivity r_a is the same in the dendrite and axon, we have

$$\lambda_1 = \sqrt{\frac{a_1}{2 g_1 r_\text{a}}}, \quad \lambda_\alpha = \sqrt{\frac{a_\alpha}{2 g_\alpha r_\text{a}}}, \quad \frac{\lambda_\alpha}{\lambda_1} = \sqrt{\frac{a_\alpha g_1}{a_1 g_\alpha}}. \tag{S42}$$

Taking $g_\alpha = g_L$ again and our earlier definition of ϵ in Eq (S39), we can write this as

$$\frac{\lambda_\alpha}{\lambda_1} = \sqrt{\epsilon \frac{a_\alpha}{a_1}}. \tag{S43}$$

Finally, for the electrically significant soma in Fig 7 we give ρ_1 but not ρ_α, noting that it can be calculated given λ_1 and λ_α or a_1 and a_α. Recalling our definitions of ρ and ϵ we find

$$\rho_1 = \frac{2\pi a_1 g_1 \lambda_1}{G_0}, \quad \rho_\alpha = \frac{2\pi a_\alpha g_\alpha \lambda_\alpha}{G_0}, \quad \frac{\rho_\alpha}{\rho_1} = \frac{1}{\epsilon} \frac{a_\alpha \lambda_\alpha}{a_1 \lambda_1}. \tag{S44}$$

Hence when λ_1 and λ_α are fixed as in Fig 7a,c,d we have

$$\frac{\rho_\alpha}{\rho_1} = \frac{1}{\epsilon^2} \frac{\lambda_\alpha^3}{\lambda_1^3}, \tag{S45}$$

while when a_1 and a_α are fixed as in Fig 7b

$$\frac{\rho_\alpha}{\rho_1} = \frac{1}{\sqrt{\epsilon}} \frac{a_\alpha^{3/2}}{a_1^{3/2}}. \tag{S46}$$

Parameter	Units	Values used/Formula
E_L	mV	-70
E_s	mV	0
μ	mV	4-12
ϵ	-	$(E_L - E_s)/(E_L + \mu - E_s)$
τ_1	ms	10
τ_α	ms	$\epsilon\tau_1$
τ_s	ms	5
λ_1	μm	200
λ_α	μm	100, 150, 200
a_α/a_1	-	$g_\alpha\lambda_\alpha^2/(g_1\lambda_1^2)$
ρ_1	-	1-16
ρ_α	-	$\rho_1\lambda_\alpha^3/(\lambda_1^3\epsilon^2)$
σ_s	mV	1-3
$v_{\rm th}$	mV	10
$v_{\rm re}$	mV	10
$x_{\rm th}$	μm	0, 30

Table S1. Parameters and their default values used in the figures present in the main text. Since many of the parameters are inter-dependent, where a value is not given, a formula for how it is derived from the other parameters is given instead.